11-2016

Distribution of Mean Kinetic Energy Around an Isolated Wind Turbine and a Characteristic Wind Turbine of a Very Large Wind Farm

Gerard Cortina
University of Utah

Marc Calaf
University of Utah

Raul Bayoan Cal
Portland State University, rcal@pdx.edu

Citation Details

Cortina, G., Calaf, M., & Cal, R. B. (2016). Distribution of mean kinetic energy around an isolated wind turbine and a characteristic wind turbine of a very large wind farm. Physical Review Fluids, 1(7), 074402.

Distribution of mean kinetic energy around an isolated wind turbine and a characteristic wind turbine of a very large wind farm

Gerard Cortina* and Marc Calaf†
Department of Mechanical Engineering, University of Utah, Salt Lake City, Utah 84112, USA

Raúl Bayoán Cal‡
Department of Mechanical Engineering, Portland State University, Portland, Oregon 97207, USA
(Received 9 March 2016; published 9 November 2016)

An isolated wind turbine and a very large wind farm are introduced into large-eddy simulations of an atmospheric boundary layer. The atmospheric flow is forced with a constant geostrophic wind and a time-varying surface temperature extracted from a selected period of the CASES-99 field experiment. A control volume approach is used to directly compare the transfer of mean kinetic energy around a characteristic wind turbine throughout a diurnal cycle considering both scenarios. For the very large wind farm case, results illustrate that the recovery of mean kinetic energy around a wind turbine is dominated by the vertical flux, regardless of atmospheric stratification. Contrarily, for an isolated wind turbine, the recovery is dependent on the background atmospheric stratification and it is produced by a combination of advection, vertical flux, and pressure redistribution. The analysis also illustrates that during the unstable stratification periods vertical entrainment of mean kinetic energy dominates, whereas during the stable regime horizontal entrainment is predominant. Finally, it is observed that in both scenarios, the single wind turbine and the large wind farm cases, turbulent mixing is driven by the background convective stratification during the unstable period and by the effect of the wind turbine during the stable regime.

DOI: 10.1103/PhysRevFluids.1.074402

I. INTRODUCTION

Wind energy has stood as a prominent element of the mix of renewable energies, with a remarkable growth of 23% over the past decade [1]. For wind energy to be profitable large arrays of wind turbines, so-called wind farms, must be built. However, the capacity for the atmospheric turbulent flow to immediately recover past a succession of wind turbines is limited, inducing power losses and enhanced structural fatigue due to turbine to turbine proximity [2–4]. In a very large wind farm, a fully developed turbulent flow develops, in which the statistical properties of the flow do not change within the horizontal directions, thus relevant changes mostly occur in the vertical direction. Within this region, the so-called wind turbine array boundary layer, the recovery of the successive turbine-generated wakes is only a result of vertical entrainment of mean kinetic energy (MKE) as shown by Lu and Porté-Agel [5], Yang *et al.* [6], VerHulst and Meneveau [7], and Abkar and Porté-Agel [8], which is a function of the wind farm arrangement [9]. This mechanism determines the overall efficiency of the farm as numerically shown by VerHulst and Meneveau [10] for a pressure-driven flow without thermal stratification, by Calaf *et al.* [11] for a neutrally stratified atmospheric flow, and experimentally by Cal *et al.* [12]. These large wind farms alter the local atmospheric flow with changes in the surface momentum and surface heat fluxes [13], as well as readjusting the Coriolis force balance [14]. Overall, wind farms increase the turbulent mixing with

*gerard.cortina@utah.edu; http://wet.mech.utah.edu
†marc.calaf@utah.edu; http://wet.mech.utah.edu
‡rcal@pdx.edu

a reduction of momentum entrainment near the surface and a large increase near the top tip of the rotor blades. These flow alterations change the heat fluxes (sensible and latent) and introduce small perturbations on the surface and air flow temperature [14–17].

A control volume approach to extend the current understanding of the redistribution of MKE and recovery process around a single wind turbine and a characteristic wind turbine of a very large wind farm has been performed during a standard diurnal cycle. Results will illustrate the differences in the redistribution of MKE according to the background atmospheric stratification (stable, unstable, and neutral), as well as the relative importance of terms contributing the MKE budget (advection, work produced by the mean pressure field gradient, MKE flux, dissipation, gravitational acceleration of vertical motions, and Coriolis forcing).

In Sec. II the control volume framework used to develop the MKE budget is introduced. Section III presents the study cases considered and Sec. IV contains the concept of the wind turbine box. Section V presents the results for the aforementioned cases, illustrating the wind turbine box approach. Finally, conclusions are outlined in Sec. VI.

II. CONTROL VOLUME ANALYSIS OF THE MEAN KINETIC ENERGY

The mean kinetic energy equation is obtained by taking the product of the mean velocity $\overline{U}_i$ and the momentum equation

$$\overline{U}_j \frac{\partial \overline{U}_i}{\partial x_j} = -\frac{1}{\rho}\frac{\partial \overline{P}}{\partial x_i} - \frac{\partial \overline{u_i' u_j'}}{\partial x_j} + \nu \frac{\partial^2 \overline{U}_i}{\partial x_j^2} + \overline{B_i} - \overline{f}_i^{\mathrm{WT}} + f_c \epsilon_{ij3} \overline{U}_j, \tag{1}$$

where the prime denotes the fluctuations and the overbar a time-averaged quantity. The mean pressure is given by $\overline{P}$ and $\overline{f}_i^{\mathrm{WT}}$ represents the force imparted on the flow by the wind turbines. The thermal buoyant forcing is represented by $\overline{B_i} = \beta g (T - T_{\mathrm{ref}})\delta_{i3}$, where β is the coefficient of thermal expansion, g is gravity, T is the mean temperature, and T_{ref} is the reference temperature. Respectively, both air flow properties, density ρ and kinematic viscosity ν, are treated as constants. The Coriolis parameter is denoted by f_c and ϵ_{ij3} is the alternating unit tensor ($\epsilon_{ij3} = 0$ if $i = j$ and ± 1 otherwise). Omission of the time dependence of the velocity field is also noted ($\partial \overline{U}_i / \partial t = 0$). After carrying out the operation, the transport equation for the mean kinetic energy $K = \frac{1}{2}\overline{U}_i^2 = \frac{1}{2}(\overline{U}^2 + \overline{V}^2 + \overline{W}^2)$ ($\overline{U}$, $\overline{V}$, and $\overline{W}$ being the streamwise, lateral, and vertical mean velocities, respectively) is obtained as

$$\begin{aligned} \overline{U}_j \frac{\partial K}{\partial x_j} =& -\frac{\partial}{\partial x_j}\left(\frac{1}{\rho}\overline{P}\,\overline{U}_i \delta_{ij} + \frac{1}{2}\overline{u_i' u_j'}\,\overline{U}_i - 2\nu \overline{S}_{ij}\overline{U}_i\right) \\ & - \overline{u_i' u_j'}\frac{\partial \overline{U}_i}{\partial x_j} - 2\nu \overline{S}_{ij}\overline{S}_{ij} + \overline{U}_i \overline{B} - \overline{U}_i \overline{f}_i^{\mathrm{WT}} + f_c \epsilon_{ij3}\overline{U}_i \overline{U}_j, \end{aligned} \tag{2}$$

where $\overline{S}_{ij} = \frac{1}{2}\left(\frac{\partial \overline{U}_i}{\partial x_j} + \frac{\partial \overline{U}_j}{\partial x_i}\right)$ is the mean strain rate tensor. From left to right, the terms in Eq. (2) are the advection of mean kinetic energy, mechanical work produced by gradients in the mean pressure field, two flux terms, i.e., mean kinetic energy by turbulence and viscous dissipation, production of turbulence kinetic energy, mean viscous dissipation, mean kinetic energy production or destruction by buoyancy forces, power extracted by the wind turbine, and the effect due to Coriolis force.

In marking a control volume (CV) around a turbine, a volume integral of the transport equation (2) is taken as shown in Fig. 1. In the CV of Fig. 1, the surfaces normal to the longitudinal direction, acting as inflow and outflow, are denoted by S_1 and S_2, lateral surfaces by S_3 and S_4, and horizontal

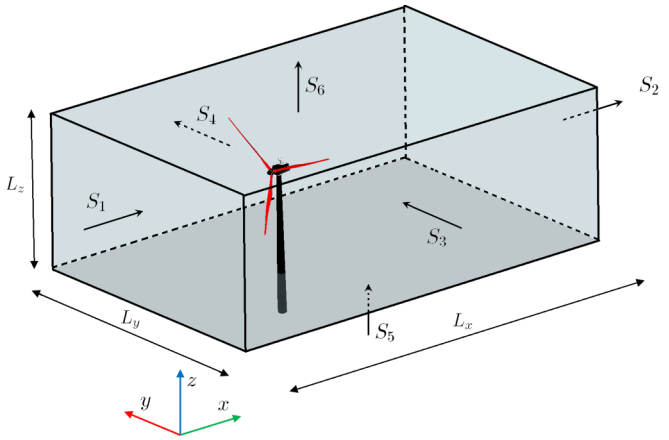

FIG. 1. Rectangular CV around the wind turbine used for an extended momentum analysis. The coordinate system denoted by x,y,z is the referent axis for the CV. The size of the CV is denoted by L_x, L_y, L_z, which represent the streamwise, spanwise, and vertical dimensions, respectively. The CV surfaces are denoted by S_i, where i indicates any of the CV surfaces (from 1 to 6).

bottom and top surfaces by S_5 and S_6. Hence, the volume integral of Eq. (2) reads

$$\overbrace{\iiint_{\forall} \overline{U}_j \frac{\partial K}{\partial x_j} d\forall}^{A_1} = -\overbrace{\iiint_{\forall} \frac{\partial}{\partial x_j}\left(\frac{1}{\rho}\overline{P}\,\overline{U}_i\delta_{ij} + \frac{1}{2}\overline{u_i'u_j'}\,\overline{U}_i - 2\nu\overline{S}_{ij}\overline{U}_i\right) d\forall}^{A_2}$$
$$- \underbrace{\iiint_{\forall} \overline{u_i'u_j'}\frac{\partial \overline{U}_i}{\partial x_j} d\forall}_{A_3} - \underbrace{\iiint_{\forall} 2\nu\overline{S}_{ij}\overline{S}_{ij} d\forall}_{A_4} + \underbrace{\iiint_{\forall} \overline{U}_i \overline{B} d\forall}_{A_5}$$
$$- \underbrace{\iiint_{\forall} \overline{U}_i\,\overline{f}_i^{\mathrm{WT}} d\forall}_{A_6} + \underbrace{\iiint_{\forall} f_c \epsilon_{ij3}\overline{U}_i\overline{U}_j d\forall}_{A_7}, \tag{3}$$

where the triple integral notation stresses that $d\forall$ is a closed volume.

To simplify the discussion, terms are labeled as A_n, where n runs from 1 to 7 as shown in the overbrackets and underbrackets in Eq. (3). Sequentially, these constitute the inertial terms A_1, the transport or flux terms denoted by A_2, production of turbulence kinetic energy A_3, and the mean viscous dissipation A_4. Finally, three-body force terms encompassing the buoyancy, the power extracted by the turbine, and the Coriolis effect, respectively, as A_5, A_6 and A_7, are also represented in Eq. (3). Introducing the divergence theorem, the volume integral of the advection of mean kinetic energy on the left-hand side is rewritten as a surface integral

$$A_1 = \iint_S (\overline{U}_i K)\hat{n}_i dS, \tag{4}$$

where $\hat{n}_i$ is the unit vector normal to the surface S of the CV. A similar treatment is applied to the volume integral of the transport terms of mean kinetic energy on the right-hand side

$$A_2 = \iint_S \left(\frac{1}{\rho}\overline{P}\,\overline{U}_i\delta_{ij} + \frac{1}{2}\overline{u_i'u_j'}\overline{U}_i - 2\nu\overline{S}_{ij}\overline{U}_i\right)\hat{n}_j dS. \tag{5}$$

Because the components of velocity tangent to the surface do not contribute to the flux across the control surface, since in such a case $\vec{u}\cdot\vec{n} = 0$, the surface integral of mean kinetic energy advection

TABLE I. Study cases for the LES numerical simulations.

Study case	ABL stratification	No. of turbines	$s_x \times s_y$
VLWF	unstable	48	$8D \times 5D$
VLWF	neutral	48	$8D \times 5D$
VLWF	stable	48	$8D \times 5D$
LSWF	unstable	1	$63D \times 31D$
LSWF	neutral	1	$63D \times 31D$
LSWF	stable	1	$63D \times 31D$

simplifies to

$$A_1 = -\iint_{S_1} \overline{U} K dS_1 + \iint_{S_2} \overline{U} K dS_2 - \iint_{S_3} \overline{V} K dS_3 + \iint_{S_4} \overline{V} K dS_4 - \iint_{S_5} \overline{W} K dS_5 + \iint_{S_6} \overline{W} K dS_6 \tag{6}$$

and surfaces are visualized in Fig. 1. Moreover, evaluating the various components within terms A_3 through A_7, the volume integral is considered. In expanding the term A_3, for example, the volume is composed of the differentials in the three directions x, y, and z and the corresponding stress term results

$$A_3 = \iiint_V \left(\overline{u'u'} \frac{\partial \overline{U}}{\partial x} + \overline{u'v'} \frac{\partial \overline{U}}{\partial y} + \overline{u'w'} \frac{\partial \overline{U}}{\partial z} + \overline{v'u'} \frac{\partial \overline{V}}{\partial x} + \overline{v'v'} \frac{\partial \overline{V}}{\partial y} + \overline{v'w'} \frac{\partial \overline{V}}{\partial z} + \overline{w'u'} \frac{\partial \overline{W}}{\partial x} + \overline{w'v'} \frac{\partial \overline{W}}{\partial y} + \overline{w'w'} \frac{\partial \overline{W}}{\partial z} \right) dx\, dy\, dz. \tag{7}$$

Therefore, it is understood that similarly it is obtained for the viscous dissipation, buoyancy, power extracted by the wind turbines, and the Coriolis terms in Eq. (3). Note that terms developed here correspond to the most general form of the MKE budget in a CV. These are correspondingly adapted to match the large-eddy simulations (see Sec. V A), which consist of a resolved and a subgrid stress contribution and neglect the viscous effects as a result of the high Reynolds number characteristic of atmospheric flows.

III. STUDY CASES

To develop this study, a suite of six large-eddy simulation (LES) cases are performed: three with a very large wind farm (VLWF) and three with a single wind turbine or largely spaced wind farm (LSWF). Table I summarizes the study cases. For both the LSWF and VLWF, a simulation consisting of a complete diurnal cycle (total of 24 h in physical time) is developed obtaining consecutive periods with stable (nighttime) and unstable (daytime) atmospheric stratification. The diurnal cycle is forced using a height-independent and time-constant geostrophic wind together with a time-varying surface temperature. The geostrophic wind $(u_G, v_G) = (9, -3)$ ms^{-1} and the surface temperature [see Fig. 2(a)] are extracted from the CASES-99 (Cooperative Atmosphere-Surface Exchange Study 1999) [18] field experiment between October 22 and 24 of 1999 and validated using results from Kumar *et al.* [19,20], Svensson *et al.* [21], and Basu *et al.* [22] as well as experimental data from the CASES-99 data set. Details on the LES framework can be found in previous works by Sharma *et al.* [23] and Cortina *et al.* [24]. The time period used to force the diurnal cycle has been previously used in studies of wind farms within a realistic atmospheric boundary layer diurnal cycle by Fitch *et al.* [25] and Sharma *et al.* [23] and is adopted here as well. Additionally, two independent cases forced with the same geostrophic forcing but with a fixed surface temperature and a well-mixed temperature profile are considered to simulate the case of a neutrally stratified atmospheric boundary layer (ABL) flow.

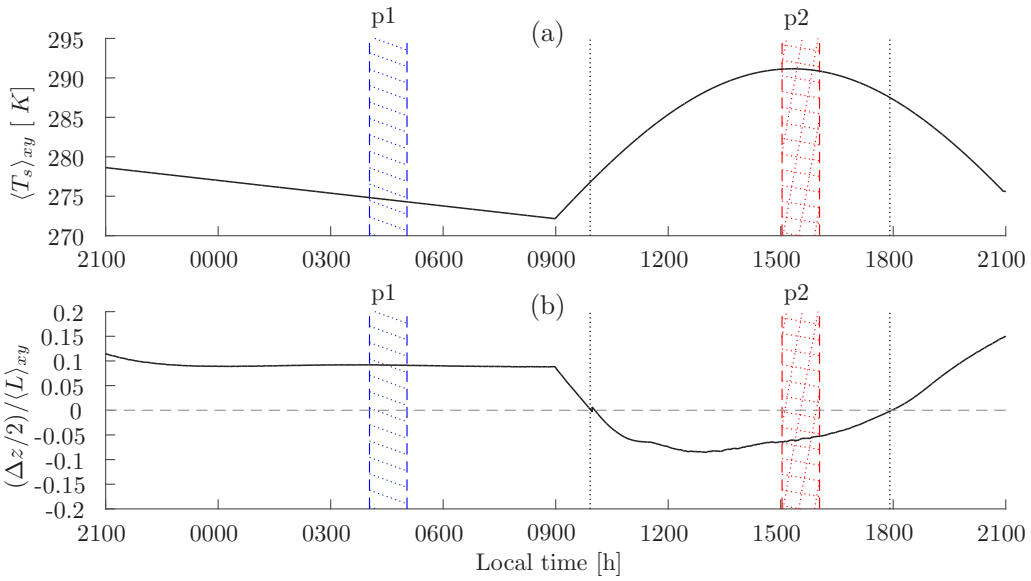

FIG. 2. (a) Horizontally averaged and time-dependent imposed temperature at the surface of the domain $\langle T_s \rangle_{xy}[K]$. (b) Normalized stability parameter $(\Delta z/2)/\langle L \rangle_{xy}$, where $\Delta z/2$ is the height of the first grid point and L is the Monin-Obukhov length as a function of time. One-hour periods marked with a 45° dotted line ($p1$), in blue, and squared dotted line ($p2$), in red, delineate time periods in which mean kinetic energy budgets and representative statistics are computed. Precisely, period $p1$ constitutes the time between 0400 and 0500 h local time (LT) and $p2$ denotes the time between 1500 and 1600 h of LT.

The time evolution of the surface temperature used to force the flow through a diurnal cycle is represented in Fig. 2(a) and the corresponding surface stability parameter z_1/L is shown in Fig. 2(b), where $z_1 = \Delta_z/2$ and Δ_z represents the vertical grid spacing. While the atmospheric flow through a diurnal cycle is intrinsically nonstationary, mean statistics over 1-h periods remain fairly unchanged. Here results for the 1-h periods between 0400 and 0500 h ($p1$) and between 1500 and 1600 h ($p2$) are presented, representative of a stable and an unstable atmospheric stratification, respectively. The same analysis is applied on other 1-h time periods through the different stable and unstable regimes, obtaining similar convergence in the statistics. A similar 1-h period is also analyzed for the neutrally stratified flow. For both cases, the LSWF and VLWF, the numerical domain is set to $(2\pi \times \pi \times 3)z_i$, where z_i is the initial height of the boundary layer, with $z_i = 1000$ m. In order to keep a high numerical resolution, the computational domain is discretized with a numerical grid of $256 \times 128 \times 384$ points, providing uniform grid resolutions of $\Delta_x = \Delta_y = 24.5$ m and $\Delta_z = 7.8$ m. The simulations are initialized with the velocity and temperature vertical profiles extracted from the CASES-99 field experiment, corresponding to a height-independent geostrophic wind and a well-mixed temperature profile matching the initial surface temperature of 278.6 K, with an inversion layer spanning from z_i to the top of the domain $3z_i$.

The VLWF configuration consists of eight rows with six wind turbines per row, using the traditional spacings of $\sim 8D$ and $\sim 5D$ (where D refers to the rotor diameter of the turbine, here taken equal to 100 m) in the streamwise and spanwise directions, respectively, as observed in Fig. 3(a). Because of the periodic boundary conditions, this configuration results in a practical sense equivalent to an infinite wind farm. On the other hand, the LSWF configuration, represented in Fig. 3(b), consists of a single wind turbine installed in the middle of the domain, and hence it is understood as a single isolated wind turbine, or as a result of the periodic boundary conditions, as a largely spaced wind farm, with wind turbine spacings of $\sim 63D$ and $\sim 31D$ in the streamwise and spanwise directions, respectively. In both configurations, the algorithm of Sharma *et al.* [26] is used

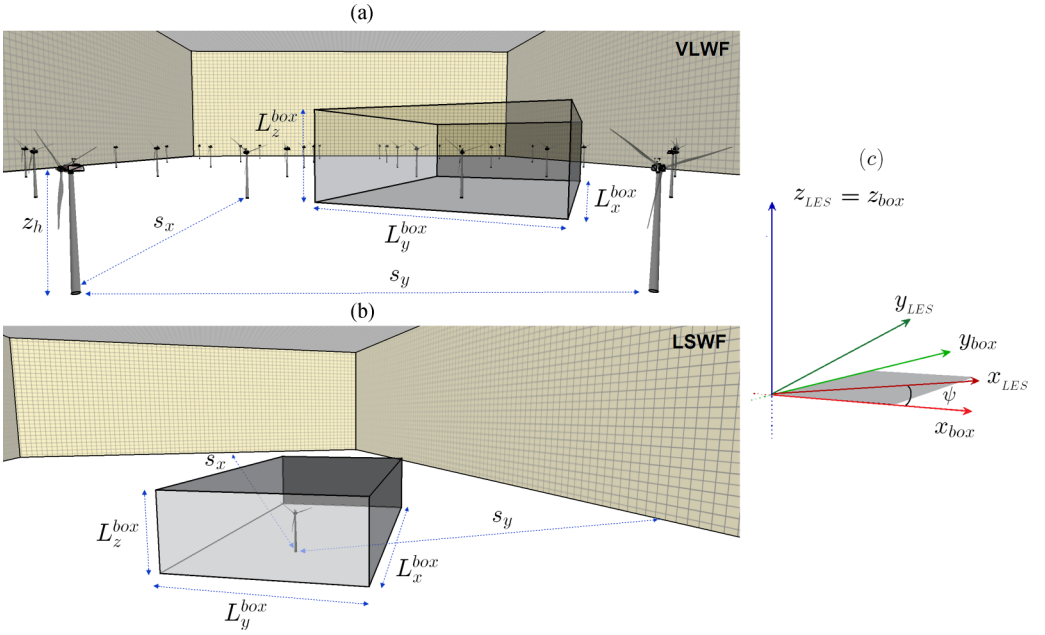

FIG. 3. (a) The VLWF case, (b) the LSWF case, and (c) graphical representation of the rotation between the LES domain coordinate frame and the wind turbine box.

to model the wind turbines, using an upstream scanning distance of $D/2$ to learn from the incoming wind vector and timely readjust the yaw angle of the turbines every 10 min (see [24]).

Differences in transport and recovery of MKE around an isolated wind turbine and a characteristic wind turbine within a wind farm are evaluated herein. To demonstrate the selected study periods, Figure 4 presents the time evolution of 10-min-averaged and horizontally averaged (between the top tip and bottom tip of the rotor) MKE for both cases, the VLWF (dashed line) and the LSWF (solid line), throughout the diurnal cycle. First, it should be noted that while the LES numerical simulation is exactly the same for both wind farms scenarios, a large difference in MKE is observed between them. During the stable stratified period (i.e., from 0000 to 0900 h), there exists ∼4 times more

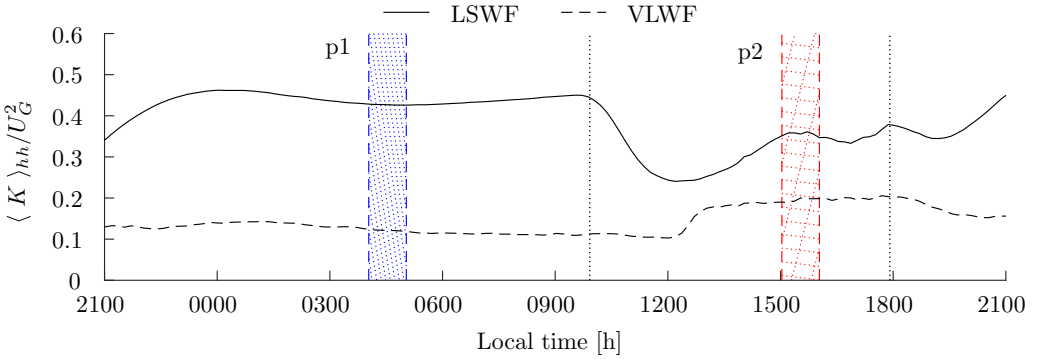

FIG. 4. Mean kinetic energy represented every 10 min and averaged over the volume capturing the wind turbine rotor disk (from $z_h - D/2$ to $z_h + D/2$, where $z_h = 100$ m is the hub height and D is the wind turbine diameter) normalized by the square of the geostrophic wind U_G. The MKE is represented for the LSWF and VLWF cases during the diurnal cycle. Correspondingly, the 45° dotted line region ($p1$), in blue, and the squared dotted region ($p2$), in red, identify the 1-h stable and unstable stratification periods.

energy in the LSWF than in the VLWF case. This is the result of the increased MKE absorption of the large wind farm. Further, the stable-LSWF period is characterized by a nocturnal low level jet (LLJ) intersecting the wind turbines rotor and hence accounted for in this MKE representation, while for the VLWF case the low level jet is shifted above the wind turbines hub layer (see [14,23,25,27]). This effect results in large energy differences between both stable conditions. On the other hand, the unstable periods are dominated by enhanced atmospheric mixing and hence the difference in available energy between the LSWF and the VLWF case is reduced. The unstable-LSWF regime (i.e., from 1300 to 1800 h) on average has 1.5 times more energy than the unstable-VLWF case. These differences in available energy will be further illustrated later within the analysis of MKE redistribution. Also, one should note the trend of MKE as a function of time. While for the LSWF more energy is available during the stable period ($K_{\text{unstable}} = 1.2K_{\text{stable}}$), for the VLWF the opposite results, with the unstable or convective regime being the one that presents the largest MKE available ($K_{\text{unstable}} = 0.5K_{\text{stable}}$). Further, it is worth noting that the MKE for the VLWF case presents a change of 30% within hours 1200 to 1400 and then reaches a quasistationary state. For the LSWF, there is an apparent constant change in the MKE ($\sim$5%/h) from 1200 to 1500 h.

IV. WIND TURBINE BOX

To directly compare the flow around a single wind turbine and the flow around a wind turbine installed within a very large wind farm, a dynamically time-realigned CV surrounding each wind turbine, from here on referred to as a wind turbine box, is developed. The wind turbine box consists of a reduced domain of adjustable size, with the box-local streamwise direction timely aligned perpendicular to the actual rotor disk [see Figs. 5(a)–5(d)]. Within this work, the box of the turbine is selected with a dimension of $(L_x^{\text{box}}, L_y^{\text{box}}, L_z^{\text{box}}) = (9D, 5D, 7D/4)$ and centered around the rotor. Precisely, the box extends between a distance of $2D$ upstream and $7D$ downstream of the disk in the streamwise direction and $2.5D$ left and right of the hub of the rotor in the cross-streamwise direction, respectively. In the vertical direction, the box is selected to extend a vertical distance between $z_h - 3D/4$ and $z_h + D$. The box size has been selected of equal size for both study cases (the VLWF and LSWF) to be able to compare statistics. Therefore, given the limited spacing in the VLWF case, the box is selected to capture the maximum wake region without including the effect of the following wind turbine. It is then possible to evaluate terms as developed in Sec. II from the standpoint of the wind turbine box as the CV is closely associated with the analysis.

The wind turbine box is designed such that its corresponding streamwise axis x_{box} is timely perpendicular to the rotor disk and hence aligned with the mean wind vector. The flow variables are initially computed within the base LES coordinate frame $(x_{\text{LES}}, y_{\text{LES}}, z_{\text{LES}})$ and then transformed into the new box coordinate frame $(x_{\text{box}}, y_{\text{box}}, z_{\text{box}})$. The mapping transformation consists of a rotation around the vertical axis $z_{\text{LES}} = z_{\text{box}}$, which remains frame invariant and it is represented by a rotation matrix, denoted by $\mathbf{R}$ with a rotation angle denoted by ψ, which represents the horizontal angle between the LES domain and box coordinate system [see Fig. 3(c)]. Note that, through the resultant coordinate transformation, the LES mean flow direction becomes the box local streamwise direction ($\vec{u}_{\text{box}} = \mathbf{R}\,\vec{u}_{\text{LES}}$). Similarly, the Reynolds stress tensor components are transformed using the corresponding matrix transformation $\tau_{\text{box}} = \mathbf{R}\,\tau_{\text{LES}}\mathbf{R}^{\text{T}}$, where $\mathbf{R}^{\text{T}}$ indicates the transpose of the rotation matrix. Figures 3(a) and 3(b) illustrate the structure of the wind turbine box within the LES domain for the VLWF and LSWF cases, respectively, and the schematics of the frame rotation $(x_{\text{LES}}, y_{\text{LES}}, z_{\text{LES}}) \rightarrow (x_{\text{box}}, y_{\text{box}}, z_{\text{box}})$ is represented in Fig. 3(c).

V. RESULTS

A. Flow around a characteristic wind turbine

Figures 5(a)–5(d) represent 1-h-averaged velocity field for both cases, the VLWF and LSWF, and for both stratification periods (stable and unstable) at hub height. In Fig. 5(a) the unstable regime causes the turbine wakes to be shorter and less organized due to the increased mixing characteristic

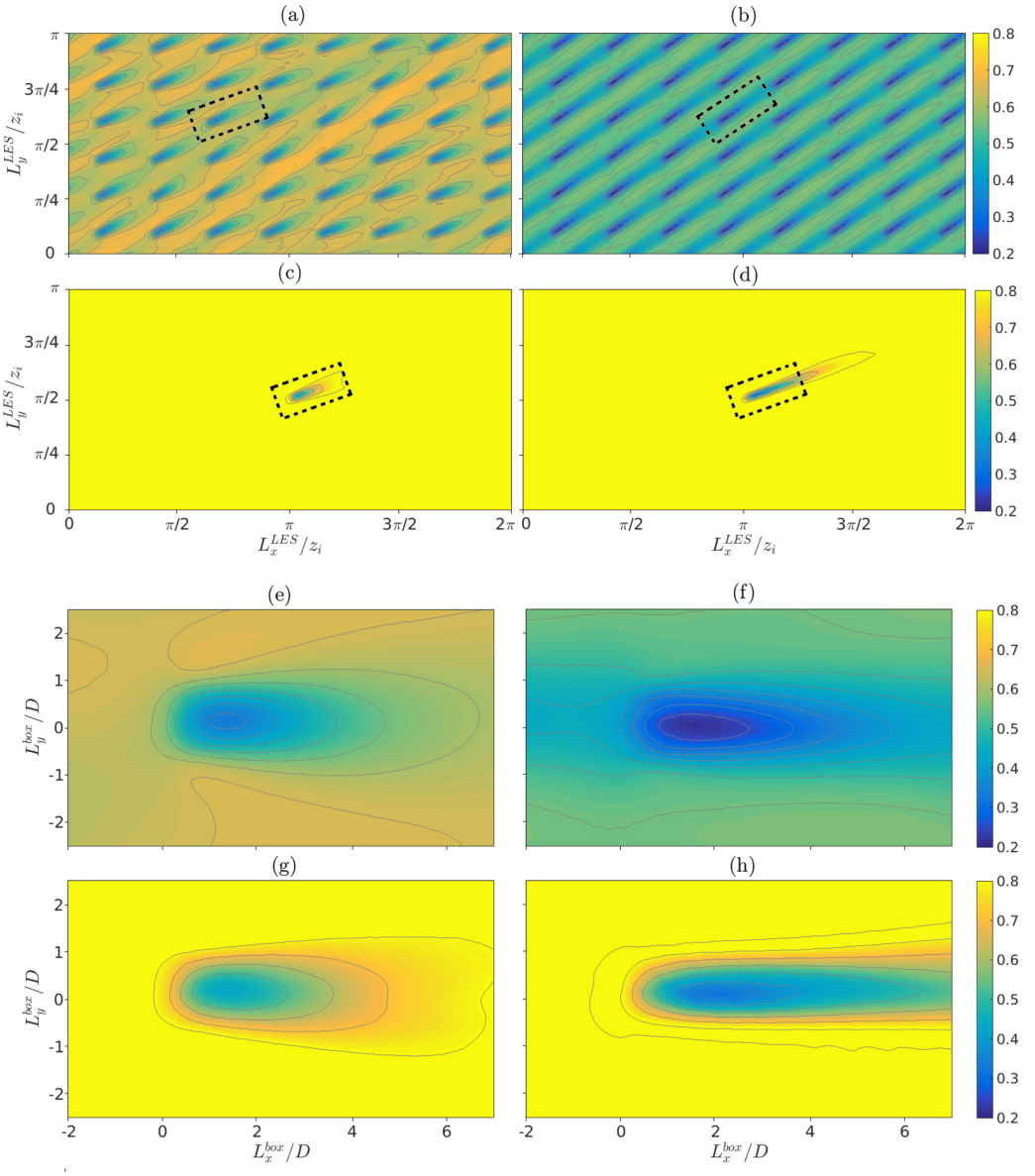

FIG. 5. The LES domain horizontal slices of 1-h-averaged, normalized velocity magnitude fields at hub height for two characteristic periods of the VLWF and LSWF simulations: (a) unstable VLWF, (b) stable VLWF, (c) unstable LSWF, and (d) stable LSWF. Also shown are the horizontal slices of 1-h averaged, normalized velocity magnitude at hub height within the wind turbine box reference frame: (e) unstable VLWF, (f) stable VLWF, (g) unstable LSWF, and (h) stable LSWF. The dashed line surrounding the wind turbine in (a)–(d) represents the wind turbine box.

of unstable regimes; this is especially the case in the VLWF. In contrast, wakes visibly persist over longer distances and overall are more organized during the stable regime [see Fig. 5(b)], as a result of the attenuated mixing due to turbulence. While the flow for the neutral stratification is not represented here, the flow shows a signature similar to that in the unstable regime, where the

turbine wakes expansion results in a radial shape, symmetrically in both directions (x-y plane), also reported by Abkar and Porté-Agel [9]. Rather than considering a wind farm, Figs. 5(c) and 5(d) highlight a single turbine under unstable and stable regimes, respectively. Wake features are similar to those in the wind farm, although these are exaggerated due to the lack of turbine-turbine wake interaction. In these cases, the difference in the expansion of the wake is in its length. Figures 5(c) and 5(d) illustrate that the length of the wake during the stable regime is twice as large as for the unstable period. Also, it should be noted that the yaw alignment has an effect on the wake length and persistence. During the 1-h stable period ($p1$) the standard deviation of the wind angle is $\sim 1^{\circ}$, while for the unstable period the standard deviation is $\sim 5^{\circ}$ (see [24]). This results in a more dynamic wind turbine force acting on the flow in time and space during the unstable regime.

Using the CV approach previously described, a comparison between the flow around a single wind turbine (LSWF) and a characteristic wind turbine within a VLWF is sought. This last one is obtained by averaging the flow of the 48-turbine boxes (one per wind turbine of the LES domain). Figure 5 presents a 1-h-averaged streamwise velocity field at hub height (using the wind turbine box) for the unstable [Figs. 5(a), 5(c), 5(e), and 5(g)] and stable [Figs. 5(b), 5(d), 5(f), and 5(h)] regimes. From this representation, the flow around both wind turbine scenarios [the VLWF represented in Figs. 5(e) and 5(f) and the LSWF represented in Figs. 5(g) and 5(h)] is very distinct between atmospheric stability conditions. From Figs. 5(e)–5(h) it can be observed that both types of turbines present different wake geometries. Flow features show changes in both streamwise and cross-streamwise directions. Figure 5(e) is the characteristic unstable wake, having a practically symmetric expansion in the horizontal direction. Figure 5(f) shows a slimmer and sharper shape with an irregular expansion, characteristic of the stable wake, as well as a velocity deficit upstream of the wind turbine, a signature of the turbine-wake interaction. Even though Fig. 5(e) should be showing a velocity deficit upstream of the wind turbine rotor, this is much more attenuated and practically nonexistent, due to the convective regime present during the unstable stratification. For the LSWF, there is no upstream velocity deficit due to the fact that in these cases there are no upstream turbines. Also, it should be noted that for the stable-VLWF case in Fig. 5(f), as a result of the overall wind reduction, the wake deficit is attenuated in comparison to the stable-LSWF case in Fig. 5(h). In general, a more rapid wake recovery is observed for the unstable-VLWF case, with the wake recovering to 90% of the inflow wind speed at $5D$ and $6D$ downstream from the rotor disk for the unstable-VLWF and unstable-LSWF cases, respectively.

B. Mean kinetic energy fluxes around a characteristic wind turbine

The MKE terms previously described in Sec. II are now redefined within the LES framework and the terms used in the following expression will be used from now on:

$$0 = A + P + \phi + \epsilon + G_a + P_{\mathrm{WT}} + C_g. \tag{8}$$

In this expression, A represents the advection term, denoted by A_1 in Eq. (3). The work due to pressure gradients on the mean flow is denoted by P and ϕ denotes the turbulent flux of MKE; these two terms correspond to the first and second terms denoted by A_2 in Eq. (3). The dissipation term, denoted by ϵ in expression (8), corresponds to the term A_3 and the gravitational acceleration of vertical motions is represented by G_a, which corresponds to the term A_5. Note that the difference between the terms A_5 and G_a [see Eq. (9)] is due to the use of the Boussinesq approximation within the LES framework. The wind turbine power extraction is identified by P_{WT} and corresponds to term A_6; finally, C_g denotes the effect of the Coriolis forcing, which corresponds to the term A_7 in Eq. (3). Notice that the third term from A_2 and the term A_6 are representative of the viscous effects, which are being neglected, as is traditional in LES of atmospheric flows because the atmospheric flow is characterized by a very large Reynolds number. Therefore, following Eqs. (2) and (3) from Sec. II, the corresponding terms of the MKE budget using the LES framework are

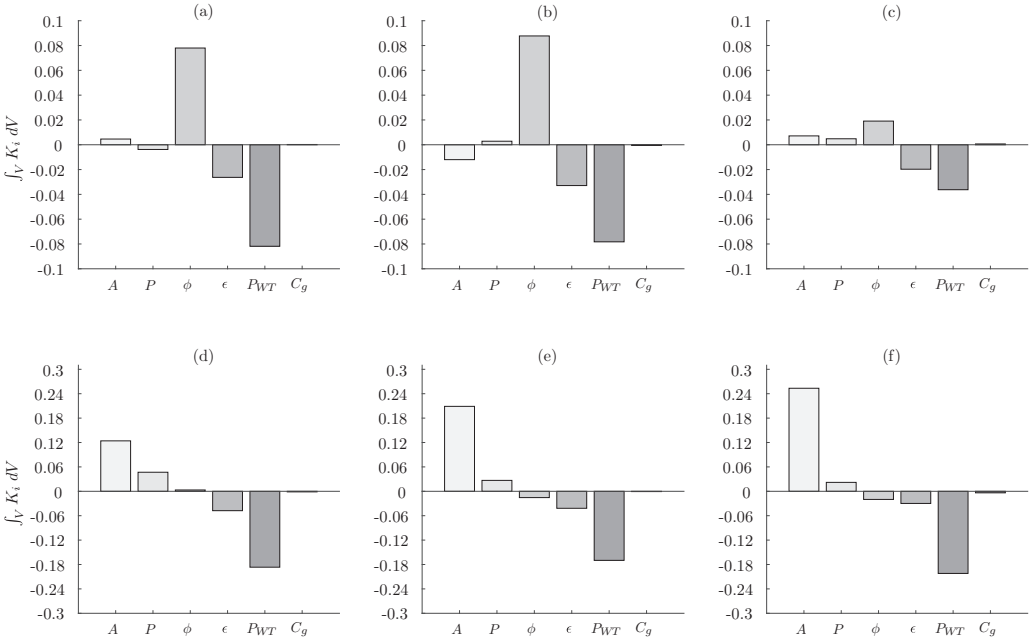

FIG. 6. Bar representation of the volume integral for the different MKE terms (K_i) within the wind turbine box. The subindex i represents the different terms contributing to the MKE budget (8), where A, P, ϕ, ϵ, P_{WT}, and C_g represent the advection, work due to pressure gradients on the mean flow, turbulent flux of MKE, dissipation, wind turbine power extraction, and the Coriolis effect, respectively. The VLWF case is shown for (a) unstable, (b) neutral, and (c) stable stratifications. The LSWF case is shown for (d) unstable, (e) neutral, and (f) stable stratifications.

represented by

$$A = -\overline{U}_j \frac{\partial K}{\partial x_j}, \quad P = -\frac{\overline{U}_i}{\rho}\frac{\partial \overline{P}}{\partial x_i}, \quad \phi = -\frac{\partial(\overline{\tau}_{ij}\overline{U}_i)}{\partial x_j}, \quad \epsilon = \overline{\tau}_{ij}\frac{\partial \overline{U}_i}{\partial x_j},$$
$$G_a = -g\left(\frac{\overline{U}_i\overline{\theta}}{\theta_{\text{ref}}}\right)\delta_{i3}, \quad P_{\text{WT}} = \overline{U}_i\overline{f}_i^{\text{WT}}, \quad C_g = f_c\epsilon_{ij3}\overline{U_iU_j}, \tag{9}$$

where $\overline{\tau}_{ij} = \overline{u_i'u_j'} + \overline{\tau}_{ij}^{\text{SGS}}$ is the sum of the Reynolds number and the subgrid scale shear stress.

Figure 6 illustrates the integral for the previously described MKE terms within the CV. This figure best illustrates the differentiated behavior in the wake recovery between the VLWF and the LSWF. For the VLWF [Figs. 6(a)–6(c)], the power harvested by the turbines corresponds to the remaining balance between the MKE dissipation and the turbulent flux of MKE; the contribution of the flux of MKE into the power harvested represents 72%, 79%, and 34% for the unstable, neutral, and stable regimes, respectively. Then it is concluded that in this case, the transport term is mainly responsible for the recovery of MKE within the turbine region, where the advection and pressure redistribution terms only provide a marginal contribution to the budget balance. In contrast, for the LSWF [Figs. 6(d)–6(f)] the harvested power is recovered mainly through the advection term (being 83%, 98%, and 109% with respect to the sum of the harvested power and dissipation for the unstable, neutral, and stable regimes, respectively) and the pressure redistribution (being 20%, 13%, and 9% with respect to the sum of the harvested power and dissipation for the unstable, neutral, and stable regimes, respectively). Note that for the LSWF scenarios the budget has a residual of 3%, 11%, and 18% for the unstable, neutral, and stable regimes, respectively. Also, it is relevant to note a factor of

2 between the advection term for the unstable [Fig. 6(d)] and stable [Fig. 6(f)] stratification cases for the LSWF cases.

This section should be concluded by stating that for the VLWF scenarios, independently of the flow stratification, the MKE is transported mainly by turbulent flux, decreased by viscous dissipation and power extracted by the wind turbine. Instead, the LSWF case is highly dependent on the stratification and differences are observed among the different regimes. While the MKE is always decreased by viscous dissipation and power extraction for the three studied stability conditions, emphasis should be placed on how the MKE is recovered or transported. While for the unstable stratification the MKE is mainly recovered within the CV by advection, pressure, and a very small contribution of turbulent flux of MKE, in the stable case the balance is practically due to advection with a very small contribution of the pressure term, with the turbulent flux having a negative contribution, also depicted in the neutral-LSWF case. In addition, the neutral case is a scenario that fits in between the unstable and stable cases.

To observe further details of the flow around an isolated wind turbine and the flow around a turbine within a large wind farm, the terms contributing to the budget of the MKE are now represented using a spatially distributed wind turbine box analysis, as presented in Sec. II. For example, Fig. 7 illustrates the contribution of the surface terms of MKE (A, ϕ, and P) through the control surface delimiting the wind turbine box, as well as horizontal slices at different heights ($z_h - D/2$, z_h, and $z_h + D/2$), of the volumetric terms contributing to the MKE budget (P_{WT}, ϵ, and C_g). The case represented in Fig. 7 corresponds to the LSWF case during the unstable regime. Influx terms to the CV are considered positive, while the outflux terms are considered negative. Each ones of the top six subplots represents a different side of the wind turbine box (front S_1, back S_2, right S_3, left S_4, bottom S_5, and top S_6 lids). The subplot located at the center represents the right plane S_3 of the box and the upper and lower ones represent the top S_6 and bottom S_5 lids, respectively. Note that these lids have the vertical axis inverted, so they perfectly connect with the right-side plane. Next the centered left and centered right subplots represent the front S_1 and back S_2 faces of the wind turbine box. Finally, the isolated, top left subplot represents the left plane of the box S_4. Within the front side, the geometry of the rotor disk is delineated with a dashed black line for the sake of reference. Note that the front plane S_1 is taken $2D$ upstream of the rotor disk.

Of special interest is the top lid subplot S_6, where an outflow of MKE can be observed from $2D$ upstream of the rotor disk to the rotor disk plane. Right behind the rotor disk, an entrainment region is observed for about $2D$ and then an outflow of MKE is measured, linked to the wake growth. An inverted behavior between the left and right sides of the wind turbine box is also present as a result of the rotation of the wake. There exists an influx at the top half of the right side of the surface S_3 with an outflux on the lower side. The opposite trend is shown on the left side, surface S_4. Finally, there is only an outflux of MKE through the back of the wind turbine box S_2. It is interesting to note that the outflux pattern is directly related to the wake of the turbine, which is vertically slanted.

To complete the picture, the spatial contribution of the MKE volumetric terms are also considered and represented through the lower 9 subplots in Fig. 7. These terms illustrate the contribution to the MKE of the Coriolis forcing (left column), the dissipation of MKE (middle column), and the power extracted by the turbines from the atmospheric flow (right column). Within each column, the different rows illustrate slices of the volume terms at different heights. From top to bottom these correspond to $z_h + D/2$, z_h, and $z_h - D/2$. In all plots, the contribution of the turbine wake and turbine rotor are quite apparent. In C_g, the turbine influences the term as two dipole features appear immediately at the rotor disk and these depend on the vertical location z, being most marked at midspan $z = z_h$. The signature in the wake is contrary to that at the rotor but with lessened magnitudes. When considering the dissipation term ϵ, once again as a function of height, it shows the signature of the rotor disk, strongly marking the lateral wind turbine effects at hub height and intensively noticeable at the center location of the wind turbine for the top and bottom plots. Finally, a significant sink is present at the exact location of the disk corresponding to the term P_{WT}. The diffuse effect of the rotor disk is due to the continuous realignment of the rotor throughout the 1-h-averaging period.

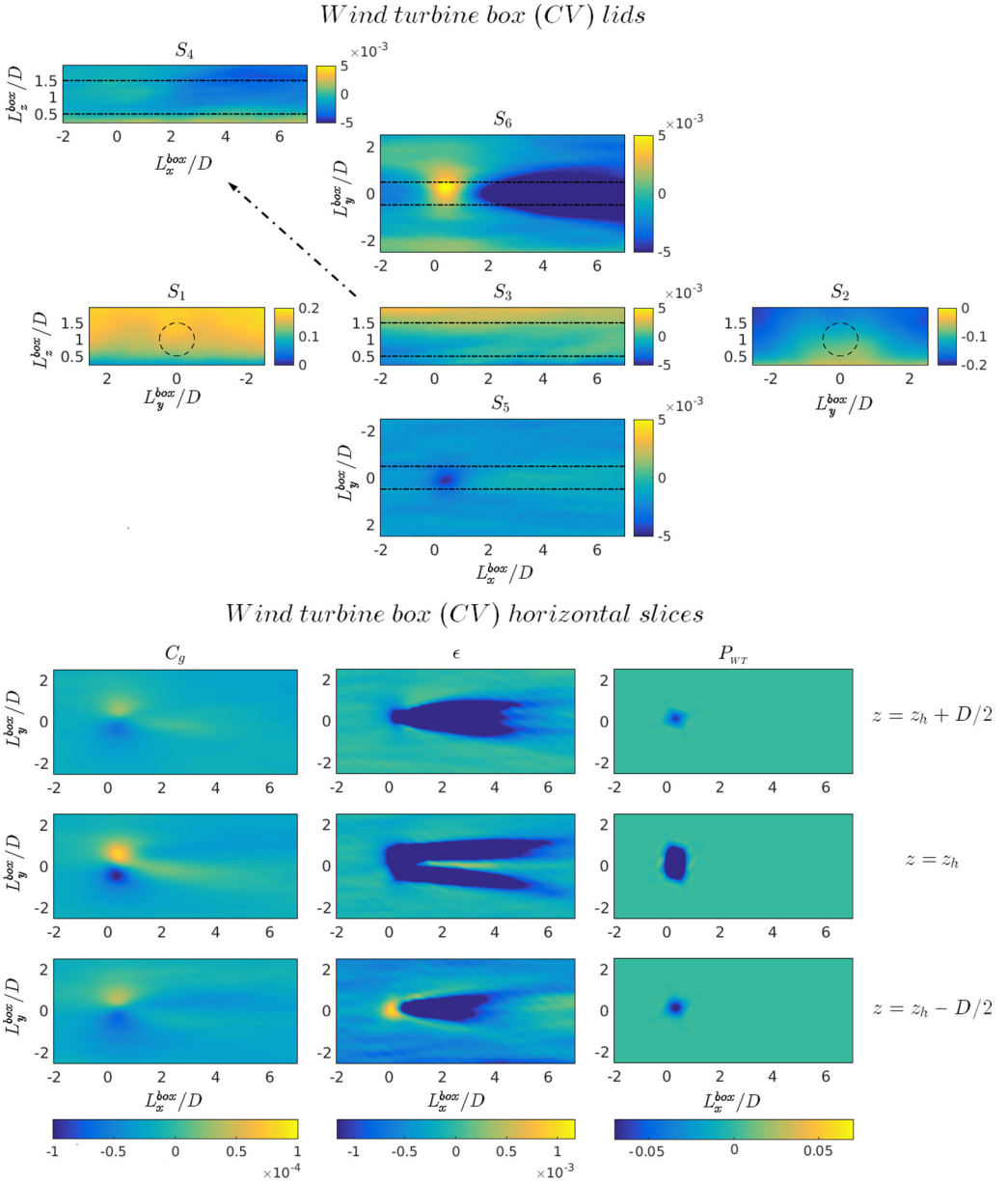

FIG. 7. Shown on top is a representation of the contribution of the surface MKE terms (sum of the advection A, turbulent flux ϕ, and pressure term P) through the control surfaces at the different lids of the wind turbine box: front S_1, back S_2, right S_3, left S_4, bottom S_5, and top S_6. Shown on the bottom are horizontal slices at different heights ($z_h - D/2$, z_h, and $z_h + D/2$) for the volume terms (C_g, ϵ, and P_{WT}) contributing to the MKE budget normalized by the geostrophic velocity and the wind turbine diameter (D/U_G^3). The top and bottom plots are representative of the 1-h averaged data for the LSWF case during the unstable regime.

In considering all cases, Fig. 8 represents streamwise profiles of the CV vertically integrated flux terms, through the lateral surfaces S_3 and S_4. Also, streamwise profiles of horizontally integrated flux terms through the bottom and top surfaces S_5 and S_6, respectively, are shown. While the wake recovery process is fully captured with this wind turbine box size for the VLWF case, for the LSWF

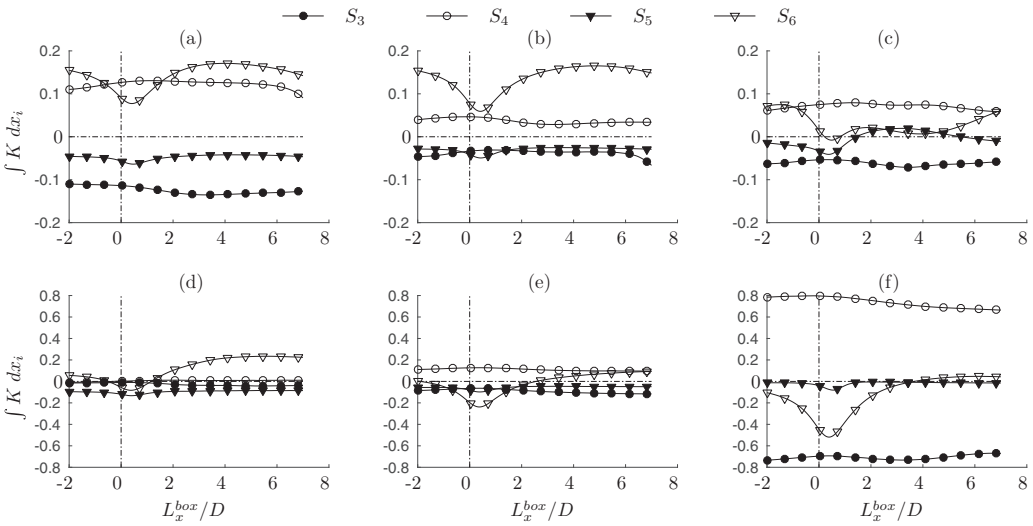

FIG. 8. Streamwise profiles of the wind turbine box, vertically integrated flux terms through the bottom S_5 and top S_6 lids and streamwise profiles of the wind turbine box horizontally integrated flux terms through the right S_3 and left S_4 surfaces. The flux terms are normalized by the cube of the geostrophic wind, the diameter of the wind turbine, and the length of the wind turbine box over which the integral is computed $D/U_G^3 L_i^{\text{box}}$, where $i = 1,3$. (a)–(c) The VLWF case and (d)–(f) the LSWF case for the unstable, neutral, and stable stratification, respectively. The vertical dashed line denotes the location of the wind turbine rotor.

case it is not, given the large extent of the wake. However, the same turbine box is used for one-to-one comparisons. Asymmetry is present in the lateral fluxes of MKE for all studied cases, meaning that the MKE entering through one side S_4 leaves almost entirely through the other side S_3 throughout the entire length of the CV. With opposite behavior, the flux of MKE through the top lid is highly dependent on the case, thus reflecting the influence of atmospheric stratification and number of turbines. For the VLWF case during the unstable regime [see Fig. 8(a)], an asymmetry exists in the MKE fluxes through the top and bottom lids. Clearly, a net influx (58% with respect to the total influx at $4D$ downstream of the wind turbine rotor) of MKE penetrates through the top lid and the flux through S_4 results in the same order of magnitude. A similar trend for the influx through the top lid S_6 is present during the VLWF neutral stratification, resulting in an influx of 84% with respect to the total influx at $4D$ downstream of the wind turbine rotor [see Fig. 8(b)]. Here a reduction of the horizontal flux is shown, being this close to 6 times smaller than the flux through S_6. Interestingly, the stable-VLWF shows a practically null vertical entrainment from the wind turbine rotor to $6D$ downstream, where the vertical MKE flux through the top lid S_6 starts to show up. This case is mainly driven by horizontal MKE flux through lid S_4. For the distinct LSWF scenarios, vertical entrainment of MKE is barely visible, except for the unstable case, where the flux through the top lid becomes important from $2D$ downstream of the rotor disk. It is interesting to note that for the stable LSWF, the horizontal flux of mean kinetic energy is remarkable, occurring along the entire length of the wind turbine box. Also, it should be noted that this case and the neutral-LSWF case are the only ones that present a negative flux through S_6 after the wind turbine rotor. This means that there exists an outflux of MKE resulting from the vertical expansion of the wake.

By integrating the MKE fluxes through the corresponding CV faces, it is possible to better quantify the relevance of the vertical entrainment of MKE in the recovery process of the depletion of MKE induced by the presence of the turbines. This is illustrated in Fig. 9 by means of a bar representation. Each bar indicates the corresponding contribution of MKE through each face of the wind turbine box (S_1, S_2, S_3, S_4, S_5, and S_6) and V represents the sum of the volume terms. As could be expected, the major inflow and outflow of MKE occurs through the front S_1 and back S_2 faces

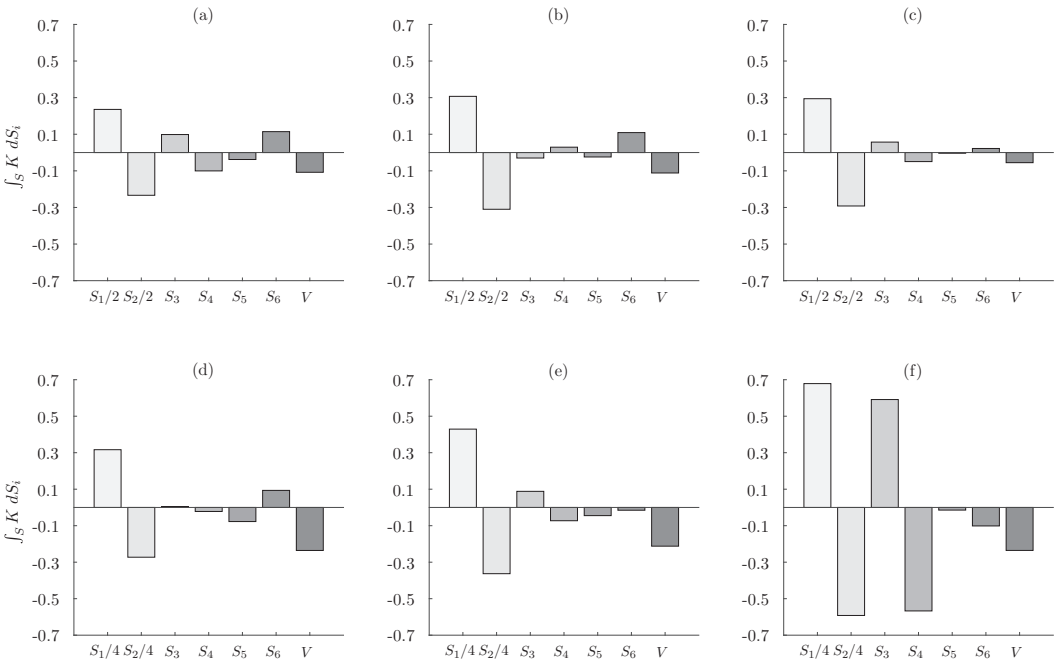

FIG. 9. Bar representation of the surface integral for the MKE flux through the distinct surfaces and volume terms. Each bar indicates the corresponding contribution of MKE through each face of the wind turbine box (S_1, S_2, S_3, S_4, S_5, and S_6) and V represents the sum of the volume terms within the control volume. The flux terms are normalized by the geostrophic wind and the diameter of the wind turbine resulting ($1/U_G^3 D^2$). The VLWF case is shown for (a) unstable, (b) neutral, and (c) stable stratification and the LSWF case is shown for (d) unstable, (e) neutral, and (f) stable stratification. Notice that for the VLWF subplots, terms S_1 and S_2 are divided by 2 and for the LSWF subplots, the same terms are divided by 4 in order to be able to visualize the magnitude of the rest of the terms.

of the wind turbine box. Note that the represented terms through faces S_1 and S_2 are divided by a factor of 2 for the VLWF and a factor of 4 for the LSWF case, for the sake of a better comparison of these terms. Furthermore, in the VLWF case these contributions are almost perfectly asymmetrical (influx S_1 versus outflux S_2) totaling to 0.48 and -0.46 for the unstable stratification [Fig. 9(a)], 0.62 and -0.62 for the neutral one [Fig. 9(b)], and 0.58 and -0.58 for the stable one [Fig. 9(c)]. Interestingly, this behavior is not as clear for the LSWF, where the values are 1.28 and -1.08 for the unstable stratification [Fig. 9(d)], 1.72 and -1.44 for the neutral one [Fig. 9(e)], and 2.72 and -2.36 for the stable one [Fig. 9(f)]. In both the VLWF and the LSWF, a similar asymmetrical behavior is observed for the lateral fluxes of MKE, as previously noted in Fig. 8, and with values of 0.1 and -0.1 for the unstable VLWF [Fig. 9(a)], -0.03 and 0.03 for the neutral VLWF [Fig. 9(b)], and 0.06 and -0.05 for the stable VLWF [Fig. 9(c)]. The unstable-LSWF case results in 0.01 and -0.02 [Fig. 9(d)], the neutral-LSWF case in 0.09 and 0.07 [Fig. 9(e)], and the stable-LSWF case in 0.59 and 0.56 [Fig. 9(f)]. Finally, attention should be focused on the asymmetric contribution of MKE through the bottom and top lids of the VLWF case (S_5 and S_6, respectively). This is the mechanism providing the recovery of most of the MKE depleted within the CV by the wind turbine, with values of -0.04 and 0.12 for the unstable case [Fig. 9(a)], -0.03 and 0.11 for the neutral one [Fig. 9(b)], and -0.004 and 0.022 for the stable one [Fig. 9(c)]. For the LSWF the contribution of MKE flux through the bottom and top lids does not greatly affect the recovery of MKE, and it can also behave as an outflux of MKE, like in the neutral and stable cases [Figs. 9(e) and 9(f)], due to the vertical slanted shape of the wake, especially during the stable regime.

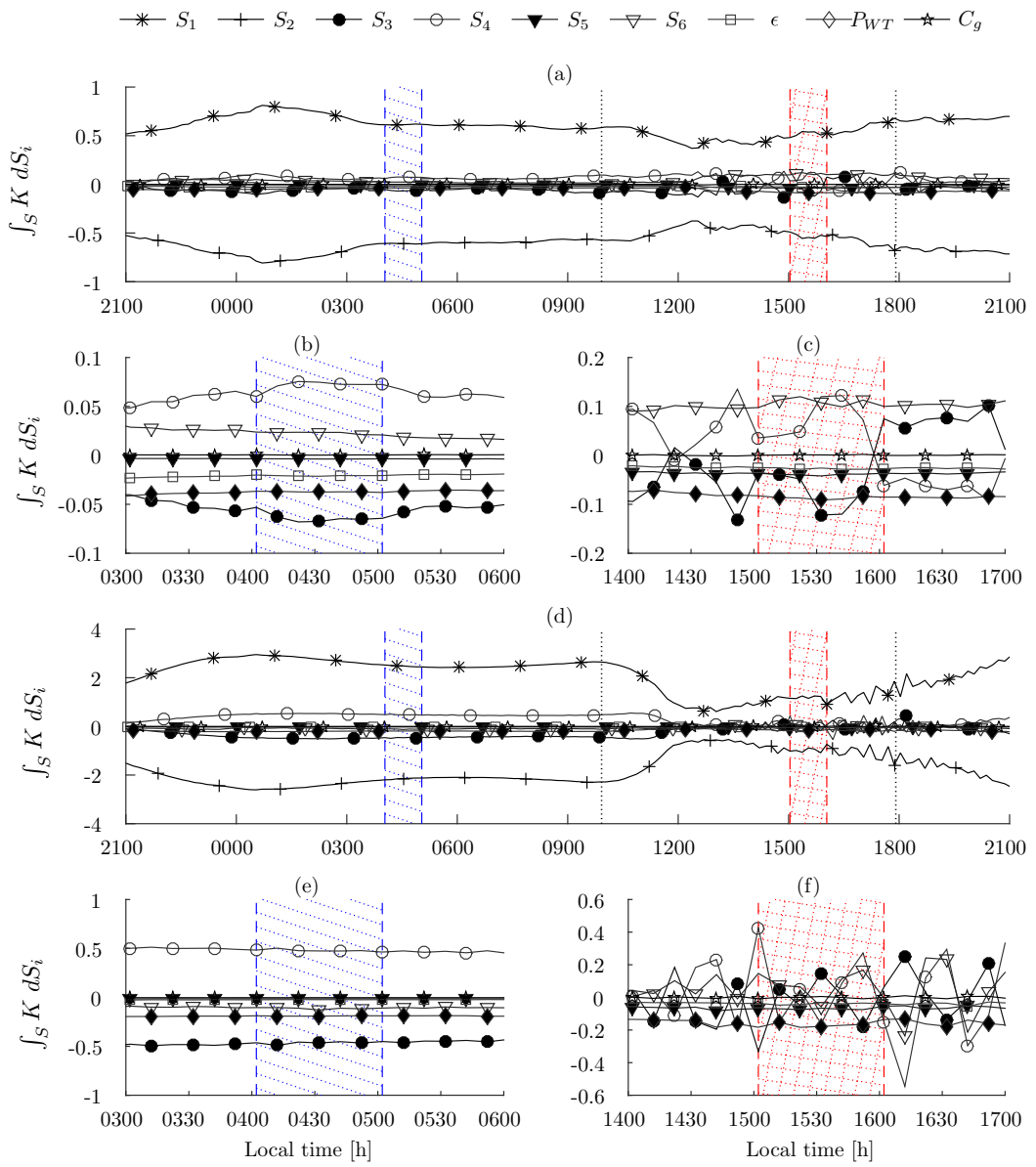

FIG. 10. Time-line representation of the 10-min-averaged surface integral for the MKE flux through the distinct surfaces (S_1, S_2, S_3, S_4, S_5, and S_6) and volume terms (ϵ, P_{WT}, and C_g) for the wind turbine box. The flux terms are normalized by the geostrophic wind and the diameter of the wind turbine resulting ($1/U_G^3 D^2$). (a)–(c) The VLWF case and (d)–(f) the LSWF case during the diurnal cycle. Notice that (b) and (c) are detailed views of the stable and unstable regimes for the VLWF case, respectively. (e) and (f) are detailed views of the stable and unstable regimes for the LSWF case, respectively.

To show the time evolution of the corresponding MKE contribution through the different surfaces of the wind turbine box, Fig. 10 represents the individualized volume terms, now averaged every 10 min instead of 1-h periods through the entire diurnal cycle. It corresponds to the previous bar plot (see Fig. 9) as a function of time and with the individualized contribution of each volume term. First, it is important to note that the behavior of the different terms does not exhibit variation as a function

of time for the represented periods (unstable and stable), illustrating that the 1-h averaging used throughout this study represents well the two different stratification regimes. Further, results illustrate that, continuously in time, the corresponding contributions through surfaces S_1 and S_2 remain the largest. It is worth noting the differentiated behavior between the VLWF and the LSWF cases: While the first almost presents negligible variation through the diurnal cycle, a more pronounced switch can be measured for the LSWF during the noon transition (between 10 a.m. and 1 p.m.) in the fluxes through S_1 and S_2. Also, for the VLWF the enhanced flux through S_5 is noticeable in comparison to S_6; $S_6 \approx 5S_5$ during the entire stable period [see Fig. 10(b)], reflecting the earlier observation that most of the wake recovery is produced as a result of the vertical transport of MKE. In contrast, for the LSWF it is the lateral flux through S_4 that contributes the most in the MKE recovery given that the fluxes through S_1 and S_2 almost perfectly compensate each other. It is also relevant to note the differentiated behavior for both cases, the VLWF and the LSWF, between the unstable and stable stratification periods, with large lateral oscillations on the fluxes through surfaces S_3 and S_4 [see Figs. 10(c) and 10(f)].

VI. SUMMARY AND CONCLUSIONS

In this work an analysis of the distribution of the mean kinetic energy around a single wind turbine (LSWF) and a characteristic wind turbine of a very large wind farm under different atmospheric stability conditions (unstable, neutral, and stable) was carried out. To accomplish a fair comparison, a dynamically yawed control volume (wind turbine box) was utilized.

The results illustrate important characteristic differences in the recovery of MKE between a VLWF and a LSWF under different atmospheric conditions. As previously shown in other studies, the harvested power by the wind turbines changes throughout the diurnal cycle, with a stronger power output during daytime and a reduction during nighttime for the VLWF (reduction of 42%). This is a result of the enhanced mixing induced by the thermal stratification during daytime and the vertical shift of the LLJ during nighttime. In contrast, for the LSWF the maximum harvested power is obtained during nighttime since the LLJ directly impinges on the rotor disk with an increase of 15%. In relation to this and for the case of a VLWF, the recovery of MKE is strongly dominated by the turbulent flux of MKE (ϕ), which presents a decreasing intensity with changing ABL stratification (a 32% and a 63% decrease for the neutral and stable stratified cases with respect to the unstable case, respectively). In contrast, for the LSWF, the recovery of MKE is shown to be dependent on the turbulent flux of MKE, the pressure redistribution term, and the advection, with advection the most important contribution. During the daytime the MKE depleted by the wind turbine is recovered by a contribution of 83% and during the nighttime the advection terms has a contribution of practically 100%. For the neutrally stratified case, again almost the totality of the MKE recovery happens through the advection.

The analysis allows us to identify the geometrical redistribution of MKE around a characteristic wind turbine. While the MKE fluxes through the front and backward faces (S_1 and S_2) are, respectively, the largest source and sink of MKE, they correspondingly compensate each other. Hence, the actual MKE recovery happens through the lateral (S_3 and S_4) and vertical (S_5 and S_6) faces of the wind turbine box. The results clearly illustrate that during the convective regime the fluxes through the vertical faces of the wind turbine box dominate, while during the stable stratification the fluxes through the lateral surfaces are most important.

Finally, the results also illustrate the fact that during the unstable regime the turbulent mixing around the wind turbines is dominated by the background atmospheric stratification, given that both the LSWF and the VLWF present a similar vertical shear at the top tip of the rotor disk (only an 8% difference). In contrast, during the nighttime, the mixing is dominated by the actual wind turbines, which is demonstrated by a much larger difference between the LSWF and VLWF vertical shear stress at the top tip of the rotor disk (a 90% difference).

ACKNOWLEDGMENTS

M.C. acknowledges the Mechanical Engineering Department at University of Utah for start-up funds. R.B.C. thanks the National Science Foundation for their support (Grant No. NSF-CBET-1034581). The authors would like to recognize the computational support provided by the Center for High Performance Computing at University of Utah.

[1] GWEC, Global Wind Report, 2014 (unpublished).
[2] N. D. Kelley and H. J. Sutherland, *Proceedings of the 35th Aerospace Sciences Meeting and Exhibit* (AIAA, Reston, NV, 1997), AIAA paper 97-0950, pp. 1–10.
[3] C. Sim, S. Basu, and L. Manuel, On space-time resolution of inflow representations for wind turbine loads analysis, Energies **5**, 2071 (2012).
[4] M. J. Churchfield, S. Lee, J. Michalakes, and P. J. Moriarty, A numerical study of the effects of atmospheric and wake turbulence on wind turbine dynamics, J. Turbul. **13**, 1 (2012).
[5] H. Lu and F. Porté-Agel, On the impact of wind farms on a convective atmospheric boundary layer, Bound.-Layer Meteor. **157**, 81 (2015).
[6] D. Yang, C. Meneveau, and L. Shen, Large-eddy simulation of offshore wind farm, Phys. Fluids **26**, 025101 (2014).
[7] C. VerHulst and C. Meneveau, Large eddy simulation study of the kinetic energy entrainment by energetic turbulent flow structures in large wind farms, Phys. Fluids **26**, 025113 (2014).
[8] M. Abkar and F. Porté-Agel, The effect of free-atmosphere stratification on boundary-layer flow and power output from very large wind farms, Energies **6**, 2338 (2013).
[9] M. Abkar and F. Porté-Agel, Mean and turbulent kinetic energy budgets inside and above very large wind farms under conventionally-neutral condition, Renew. Energ. **70**, 142 (2014).
[10] C. VerHulst and C. Meneveau, Altering kinetic energy entrainment in large eddy simulations of large wind farms using unconventional wind turbine actuator forcing, Energies **8**, 370 (2015).
[11] M. Calaf, C. Meneveau, and J. Meyers, Large eddy simulation study of fully developed wind-turbine array boundary layers, Phys. Fluids **22**, 015110 (2010).
[12] R. B. Cal, J. Lebrón, L. Castillo, H. S. Kang, and C. Meneveau, Experimental study of the horizontally averaged flow structure in a model wind-turbine array boundary layer, J. Renew. Sustain. Energ. **2**, 013106 (2010).
[13] M. Calaf, M. B. Parlange, and C. Meneveau, Large eddy simulation study of scalar transport in fully developed wind-turbine array boundary layers, Phys. Fluids **23**, 126603 (2011).
[14] H. Lu and F. Porté-agel, Large-eddy simulation of a very large wind farm in a stable atmospheric boundary layer, Phys. Fluids **23**, 065101 (2011).
[15] F. Porté-Agel, H. Lu, and Y. Wu, *23rd International Congress of Theoretical and Applied Mechanics* (Elsevier, Amsterdam, 2014), Vol. 10, pp. 307–318.
[16] B. Witha, G. Steinfeld, M. Dörenkämper, and D. Heinemann, Large-eddy simulation of multiple wakes in offshore wind farms, J. Phys.: Conf. Ser. **555**, 012108 (2014).
[17] M. Dörenkämper, B. Witha, G. Steinfeld, D. Heinemann, and M. Kühn, The impact of stable atmospheric boundary layers on wind-turbine wakes within offshore wind farms, J. Wind Eng. Ind. Aerodyn. **144**, 146 (2015).
[18] G. S. Poulos, W. Blumen, D. C. Fritts, J. K. Lundquist, J. Sun, S. P. Burns, C. Nappo, R. Banta, R. Newsom, J. Cuxart, E. Terradellas, B. Balsley, and M. Jensen, CASES-99: A comprehensive investigation of the stable nocturnal boundary layer, Bull. Am. Meteor. Soc. **83**, 555 (2002).
[19] V. Kumar, G. Svensson, A. A. M. Holtslag, C. Meneveau, and M. B. Parlange, Impact of surface flux formulations and geostrophic forcing on large-eddy simulations of diurnal atmospheric boundary layer flow, J. Appl. Meteor. Climat. **49**, 1496 (2009).

[20] V. Kumar, J. Kleissl, C. Meneveau, and M. B. Parlange, Large-eddy simulation of a diurnal cycle of the atmospheric boundary layer: Atmospheric stability and scaling issues, Water Resour. Res. **42**, 1 (2006).
[21] G. Svensson *et al.*, Evaluation of the diurnal cycle in the atmospheric boundary layer over land as represented by a variety of single-column models: The second GABLS experiment, Bound.-Layer Meteor. **140**, 177 (2011).
[22] S. Basu, J. F. Vinuesa, and A. Swift, Dynamic LES modeling of a diurnal cycle, J. Appl. Meteor. Climat. **47**, 1156 (2007).
[23] V. Sharma, M. B. Parlange, and M. Calaf, Perturbations to the spatial and temporal characteristics of the diurnally-varying atmospheric boundary layer due to an extensive wind farm, Bound.-Layer Meteor. **161**, 1 (2016).
[24] G. Cortina, V. Sharma, and M. Calaf, Investigation of the incoming wind vector for improved wind turbine yaw-adjustment under different atmospheric and wind farm conditions, Renew. Energ. **101C**, 376 (2017).
[25] A. C. Fitch, J. K. Lundquist, and J. B. Olson, Mesoscale influences of wind farms throughout a diurnal cycle, Mon. Weather Rev. **141**, 2173 (2013).
[26] V. Sharma, M. Calaf, M. Lehning, and M. B. Parlange, Time-adaptive wind turbine model for an LES framework, Wind Energy **19**, 939 (2016).
[27] M. Abkar, A. Sharifi, and F. Porté-Agel, Wake flow in a wind farm during a diurnal cycle, J. Turbul. **17**, 420 (2016).